

Low-temperature rheology of calcite

Michael K. Sly,¹ Arashdeep S. Thind,² Rohan Mishra,^{2,3} Katharine M. Flores^{2,3} and Philip Skemer¹

¹*Department of Earth and Planetary Sciences, Washington University in Saint Louis, 1 Brookings Dr, St. Louis, MO 63130, USA. E-mail: msly@wustl.edu*

²*Institute of Materials Science and Engineering, Washington University in Saint Louis, 1 Brookings Dr, St. Louis, MO 63130, USA*

³*Department of Mechanical Engineering and Materials Science, Washington University in Saint Louis, 1 Brookings Dr, St. Louis, MO 63130, USA*

Accepted 2019 December 20. Received 2019 December 19; in original form 2019 April 24

SUMMARY

Low-temperature plastic rheology of calcite plays a significant role in the dynamics of Earth's crust. However, it is technically challenging to study plastic rheology at low temperatures because of the high confining pressures required to inhibit fracturing. Micromechanical tests, such as nanoindentation and micropillar compression, can provide insight into plastic rheology under these conditions because, due to the small scale, plastic deformation can be achieved at low temperatures without the need for secondary confinement. In this study, nanoindentation and micropillar compression experiments were performed on oriented grains within a polycrystalline sample of Carrara marble at temperatures ranging from 23 to 175 °C, using a nanoindenter. Indentation hardness is acquired directly from nanoindentation experiments. These data are then used to calculate yield stress as a function of temperature using numerical approaches that model the stress state under the indenter. Indentation data are complemented by uniaxial micropillar compression experiments. Cylindrical micropillars ~ 1 and ~ 3 μm in diameter were fabricated using a focused ion beam-based micromachining technique. Yield stress in micropillar experiments is determined directly from the applied load and micropillar dimensions. Mechanical data are fit to constitutive flow laws for low-temperature plasticity and compared to extrapolations of similar flow laws from high-temperature experiments. This study also considered the effects of crystallographic orientation on yield stress in calcite. Although there is a clear orientation dependence to plastic yielding, this effect is relatively small in comparison to the influence of temperature.

Key words: Creep and deformation; Plasticity, diffusion, and creep; Rheology: crust and lithosphere.

1 INTRODUCTION

Calcite is a common rock-forming mineral in the upper crust and plays a major role in crustal deformation and rheology. While calcite may deform by one of several mechanisms there is abundant microstructural evidence for viscoplastic deformation at shallow conditions, within calcite-rich faults and shear zones. Over temperatures ranging from 100 to 500 °C natural calcite exhibits deformation microstructures that include twins and intracrystalline dislocations (Vernon 1981; Kennedy & White 2001; De Bresser *et al.* 2002; Liu *et al.* 2002; Rybacki *et al.* 2011; Wells *et al.* 2014; Kim *et al.* 2018; Negrini *et al.* 2018). At temperatures less than 400 °C ($T/T_m \approx 0.3$), deformation of calcite is dominated by twinning (Ferrill *et al.* 2004). Twinning on $e\{10\bar{1}8\}\{40\bar{4}1\}$ is common in calcite at low temperatures because it has a small critical resolved shear stress and is only weakly temperature-dependent (Burkhard 2000). However, if an individual crystal is unfavorably oriented for twinning, other slip systems, including slip on $r\{10\bar{1}4\}\{2\bar{0}21\}$ and

$f\{\bar{1}012\}\{2\bar{0}21\}$, can be activated at low temperatures (De Bresser & Spiers 1997). There is also evidence of other deformation processes at low temperature such as crystal plasticity or recrystallization-accommodated dislocation creep (Vernon 1981; Kennedy & White 2001; De Bresser *et al.* 2002; Liu *et al.* 2002; Rybacki *et al.* 2011) and grain boundary sliding (Wells *et al.* 2014; Negrini *et al.* 2018).

Numerous experiments have been performed to characterize the rheology of calcite over a wide range of pressure, temperature and stress states. Deformation experiments in compression and tension have been conducted on single crystals (Turner *et al.* 1954; Griggs *et al.* 1960; De Bresser & Spiers 1990, 1997; De Bresser *et al.* 1993; De Bresser 1996) and polycrystalline samples (Rowe & Rutter 1990; Rutter 1995; De Bresser 1996; Renner *et al.* 2002; Platt & De Bresser 2017), at temperatures of 20–1000 °C and confining pressures of 0.2–1.0 GPa. Additional experiments in direct shear (Schmid *et al.* 1987; Verberne *et al.* 2013) and torsional geometries (Pieri, Burlini, *et al.* 2001; Pieri, Kunze, *et al.* 200; Barnhoorn *et al.*

2004; Schuster *et al.* 2017) have been conducted on polycrystalline samples at temperatures of 25 to ~ 1500 °C and confining pressures of 0.2–6.0 GPa.

Despite the microstructural evidence for viscoplastic deformation in natural calcite samples deformed at shallow crustal depths (corresponding to temperatures of 100–500 °C), most laboratory experiments have been performed at temperatures greater than 300 °C. Indeed, only a handful of studies report results from experiments below 300 °C (Turner *et al.* 1954; Schmid *et al.* 1987; Rowe & Rutter 1990; Verberne *et al.* 2013; Schuster *et al.* 2017). High temperatures are commonly used in rock deformation experiments to promote thermally activated processes including diffusion and dislocation creep at laboratory strain rates that are greater than tectonic strain rates. High pressures are also needed to suppress fracturing. Low-temperature flow laws are therefore mainly constrained through the extrapolation of data from higher temperatures (e.g. De Bresser & Spiers 1997; De Bresser *et al.* 2002; Renner *et al.* 2002; Mei *et al.* 2010). This extrapolation increases the uncertainty in any modeling or inference of deformation conditions of calcite-rich rocks deformed in shallow crustal faults and shear zones (e.g. Hirth & Kohlstedt 2015).

In this study, we determine directly the rheology of calcite at low temperatures (23–175 °C) using micromechanical methods, including instrumented nanoindentation and micropillar compression. In a nanoindentation experiment, a sharp probe is pushed into the material of interest at a constant loading rate or a constant displacement rate, referred to as load-control and displacement-control, respectively (Oliver & Pharr 1992, 2004; VanLandingham 2003). Simultaneous records of load and probe displacement are used to determine the mechanical response of the sample. Nanoindentation facilitates the study of plastic deformation in geologic materials at low temperatures because the self-confined nature of the experiment suppresses fracturing (Goldsby *et al.* 2004; Kearney *et al.* 2006; Kranjc *et al.* 2016; Kumamoto *et al.* 2017; Thom & Goldsby 2019). Nanoindentation experiments are also quick in comparison to other rock deformation experiments, facilitating the collection of large data sets (e.g. >2000 individual deformation experiments in this study). However, the complex stress state below the indenter tip presents a challenge when uniaxial properties are desired, necessitating a numerical analysis to obtain material properties such as yield stress.

Nanoindentation can be complemented by additional micropillar compression tests, which enable the direct measurement of uniaxial yield stress at length scales similar to those in nanoindentation experiments. In a micropillar compression experiment, a micron-scale pillar is micromachined using a focused ion beam (FIB) and then deformed in uniaxial compression using a flat probe (Uchic *et al.* 2009). Due to the small size of the pillar, brittle processes are suppressed and viscoplastic deformation may be observed (Korte & Clegg 2009; Korte-Kerzel 2017). In this study, we use data from both nanoindentation and micropillar compression experiments to elucidate the rheology of calcite at low temperatures that are relevant to geological studies and geodynamic modeling of crustal rheology and orogenesis.

2 METHODS

2.1 Specimen preparation and initial characterization

Indentation experiments were conducted within individual grains of a single polycrystalline sample of Carrara marble, which has

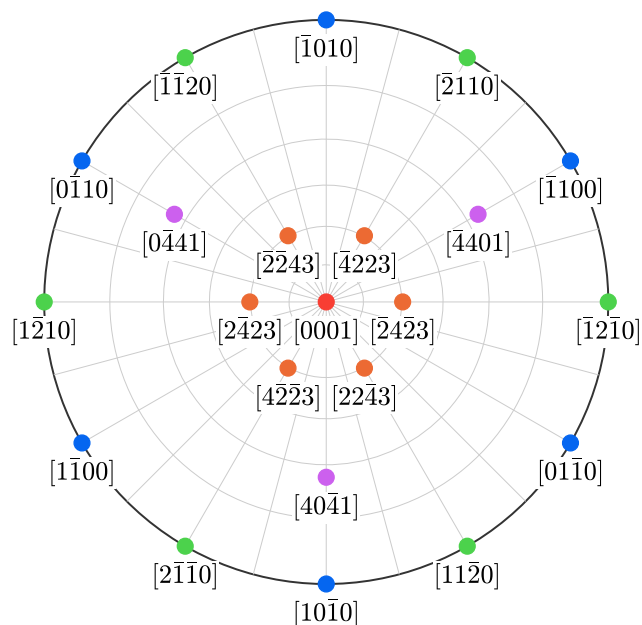


Figure 1. Equal angle, upper hemisphere, antipodal pole figure showing the crystallographic orientations used in this study. Colors correspond to crystal orientation and are the same colors used in Figs 3–6. All grains chosen for testing are oriented such that one of the directions shown here is within 10° of the indentation direction.

an average grain size of 100–200 μm . A $7 \times 9 \times 1$ mm sample was cut from a larger block that has been widely used in rock deformation studies (e.g. Fredrich *et al.* 1989, 1990; Xu & Evans 2010), and polished using progressively finer diamond grit, with a final polish using 0.02 μm colloidal silica. Crystallographic orientations of individual grains were determined using an Oxford Instruments Electron Backscatter Diffraction (EBSD) system on a JEOL 7001 FLV scanning electron microscope (SEM), operating at an accelerating voltage of 20 kV and working distance of 19 mm. For this study, grain orientation is defined by the crystallographic direction parallel to the direction of indentation. These orientations were selected to maintain consistency with previous experiments by Turner *et al.* (1954) and De Bresser & Spiers (1997), both of which investigated the orientation dependence of twinning in calcite. Five crystallographic orientations were chosen for indentation experiments: [0001], (11 $\bar{2}$ 0), (10 $\bar{1}$ 0), (22 $\bar{4}$ 3) and (40 $\bar{4}$ 1) (Fig. 1). [0001] corresponds to the *c*-axis of the calcite grain, while (11 $\bar{2}$ 0) and (10 $\bar{1}$ 0) correspond to the *a*-axes and the poles to mirror planes, respectively; these two orientations are normal to the *c*-axis. Crystals deformed parallel or subparallel to [0001] are oriented unfavorably for twinning, while crystals deformed normal to the *c*-axis ((11 $\bar{2}$ 0) and (10 $\bar{1}$ 0)) are oriented favorably for twinning on $e\{10\bar{1}8\}$ (40 $\bar{4}$ 1) under uniaxial compression (Turner *et al.* 1954; De Bresser & Spiers 1997). The two remaining orientations, (22 $\bar{4}$ 3) and (40 $\bar{4}$ 1), are also unfavorable for twinning under uniaxial compression (De Bresser & Spiers 1997). Twenty-four grains, including four to five grains in each orientation defined above, were chosen for testing. Due to the weak texture of Carrara marble and the paucity of ideal matches to the desired orientations, the grains chosen for this study are within 10° of a desired orientation. We do not account for the azimuthal orientation of the grain with respect to the faces of the three-sided pyramidal indenter. Differences in azimuthal orientation of grains may introduce small scatter in our results, which is on the order of 5%.

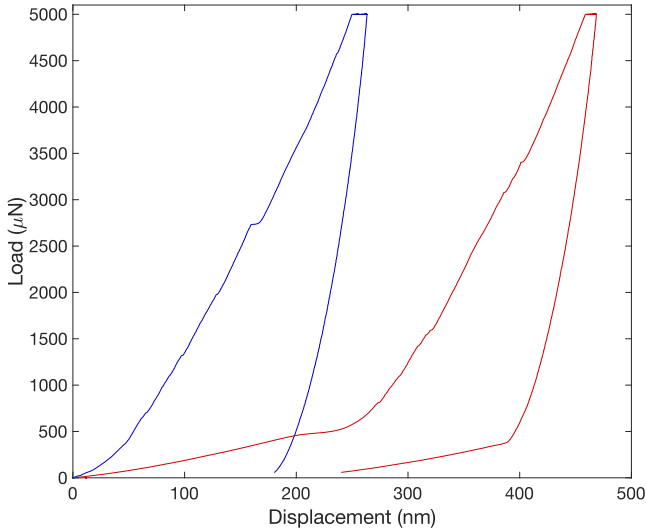


Figure 2. Load-displacement curves for high quality (blue) and poor quality (red) indentations from the same grain at the same temperature. Typical load displacement curves have continuous curvature, and occasionally show few, small increases in displacement ($\sim 1\text{--}10$ nm) referred to as pop ins. A small change in displacement at the maximum load results from creep during the 2 s hold in the loading function. Load functions that deviate from this shape often imply that the data are not useful and are not used in this study.

2.2 Nanoindentation

Load-controlled nanoindentation experiments in this study were performed using a diamond Berkovich indenter probe in a Hysitron TI 950 TriboIndenter equipped with a temperature control stage. Individual indentation experiments consist of three segments: 5 s of loading at a constant rate to the maximum load of 5 mN, a 2-s hold at the maximum load and 5 s of unloading at a constant rate. We use a maximum load of 5 mN to ensure contact depths are sufficiently deep to avoid complications with misshapen or blunted indenter tips. The indentation load, P , and probe displacement, h , are recorded simultaneously during each indentation experiment (Fig. 2). Load measurements have a nominal precision of <1 nN and displacement measurements have a precision of <0.02 nm.

The probe displacement is then converted to contact depth, h_c , for each indent using the maximum load applied, P_{\max} , and the initial unloading contact stiffness, S , which is determined from the slope of the initial portion of the unloading curve.

$$h_c = h - 0.75 \frac{P_{\max}}{S} \quad (1)$$

Contact area is related to contact depth through a polynomial function of the form:

$$A_c = a_0 h_c^2 + a_1 h_c + a_2 h_c^{1/2} + a_3 h_c^{1/4} + \dots, \quad (2)$$

where a_i are constants determined by indenting a material with well-known indentation hardness and reduced elastic modulus over a wide range of loads. Fused silica was indented over the range of $100\text{--}10\,000$ μN for this calibration. Indentation hardness, H , and reduced elastic modulus, E_r , are calculated for each indent using eqs (3) and (4), respectively, and compared to the known values to determine the accuracy of the area function.

$$H = \frac{P_{\max}}{A_c} \quad (3)$$

$$E_r = \frac{S\sqrt{\pi}}{2\sqrt{A_c}}. \quad (4)$$

The area function is considered acceptable if the calculated values are within 10% of the known values.

The measured load and displacement, along with the contact area, are used to calculate the indentation hardness and the reduced elastic modulus of the indented material. The reduced elastic modulus is related to Young's modulus by:

$$\frac{1}{E_r} = \left(\frac{1 - \nu^2}{E} \right)_{\text{sample}} + \left(\frac{1 - \nu^2}{E} \right)_{\text{indenter}}, \quad (5)$$

where E is Young's modulus and ν is Poisson's ratio, and the subscripts refer to the properties of the sample and the indenter tip. The Young's modulus and Poisson's ratio for the diamond indenter are 1140 GPa and 0.07, respectively.

The shape of the load–displacement curve is used to assess the quality of the data (Fig. 2). Indents with atypical load–displacement curves may indicate that the probe tip encountered something other than the flat sample surface (e.g. defects, debris on the sample or surface roughness) and are excluded from subsequent analysis.

Between 20 and 25 indents were made in each grain at four temperatures (23, 75, 125 and 175 $^{\circ}\text{C}$) resulting in approximately 100 indents in each grain and over 2000 indents in total. The volume affected by each indent extends beyond the contacted area and individual indents were spaced 10 μm apart to avoid interaction between indents. For experiments at all temperatures the sample was clamped to the stage and allowed to equilibrate to the desired temperature for at least 30 min prior to the start of the experiment. After the indents were completed, the structure and morphology of individual indents were examined *in situ* using Scanning Probe Microscopy (SPM) in the Hysitron TI 950 TriboIndenter, as well as *ex situ* using SEM. SPM produces topographical images by scanning the nanoindenter probe across the sample while maintaining a constant load between the probe and the surface. SPM images were taken of representative indentations in each orientation. Using the SEM, secondary electron images were taken of representative indents produced at each temperature and orientation.

2.3 Micropillar compression

Micropillars were fabricated using a focused ion beam (FIB) micromilling technique that was originally developed and applied to metallic materials (Uchic *et al.* 2009). Two instruments were used: a Zeiss Crossbeam 540 FIB-SEM and an FEI Quanta 3D FEG. Prior to fabricating micropillars, the entire Carrara marble sample was coated with iridium to avoid sample charging. The Ga^+ ion beam was then used to sputter away small amounts of the sample material in concentric annular rings to produce a well with a cylindrical pillar at the centre. To minimize ion implantation damage, the pillars are machined using progressively smaller concentric rings with progressively lower ion beam doses to produce a 25 μm diameter well with a 1 or 3 μm diameter pillar in the centre. The micropillars have an approximate diameter to height ratio of 1:2. Multiple micropillars were made in several grains oriented for compression parallel to $\langle 22\bar{4}3 \rangle$ (unfavorably oriented for twinning), and for compression parallel to $\langle 10\bar{1}0 \rangle$ and $\langle 11\bar{2}0 \rangle$ (favorably oriented for twinning).

Micropillar compression experiments were conducted in load control using monotonic, stair-step loading functions with alternating segments of loading and holding. Experiments were stopped

when a sharp change in displacement with respect to time was observed, which was assumed to coincide with the onset of brittle failure or plastic yielding. The load at which yielding occurred is converted to yield stress by:

$$\sigma_y = \frac{P_y}{A_p}, \quad (6)$$

where P_y is the load at the time of failure or yielding and A_p is the area of the top of the micropillar prior to testing.

2.4 Scanning transmission electron microscopy

A thin foil from a deformed micropillar was prepared using a Hitachi NB5000 focused ion and electron beam system. The top of the micropillar was coated with a 1- μm -thick layer of carbon followed by a 1- μm -thick layer of platinum. Additionally, a 2- μm -thick platinum coating was deposited to protect both sides of the micropillar from collapsing during FIB lift-out. A 20 kV beam with 0.7 nA current was used to cut the foil from the base of the micropillar, while beam currents of 0.07 nA at 10 kV and 0.01 nA at 5 kV were used to perform rough and fine milling, respectively, to make the foil electron transparent. The resulting foil was mounted on a Cu grid for scanning transmission electron microscopy (STEM) experiments.

STEM imaging was carried out using the aberration-corrected Nion UltraSTEMTM 200 (operating at 200 and 100 kV) at Oak Ridge National Laboratory, which is equipped with a fifth-order aberration corrector and a cold-field emission electron gun. The Cu grid was baked at 160 °C under vacuum prior to the STEM experiments to remove organics.

3 RESULTS

3.1 Nanoindentation

The indentation hardness of calcite varies systematically with crystallographic orientation (Table 1 and Fig. 3). Grains indented parallel ($[0001]$) and subparallel ($\langle 22\bar{4}3 \rangle$) to the c -axis, are harder than those indented normal to the c -axis ($\langle 11\bar{2}0 \rangle$ and $\langle 10\bar{1}0 \rangle$). The fifth orientation tested ($\langle 40\bar{4}1 \rangle$), which lies between the c -axis $[0001]$ and $\langle 10\bar{1}0 \rangle$, exhibits intermediate hardness. Differences between grains of similar orientations are assumed to be due to small misalignments of grains with respect to the indenter.

At room temperature (23 °C) grains with hard orientations, parallel or subparallel to the c -axis, have an average hardness of 2.82 ± 0.12 – 2.86 ± 0.13 GPa. Grains in softer orientations have an average hardness of 2.59 ± 0.10 – 2.60 ± 0.09 GPa. Anisotropy of hardness, A_H , is defined as:

$$A_H = \left(\frac{H_{\max} - H_{\min}}{H_{\text{all}}} \right) \times 100, \quad (7)$$

where H_{\max} is the average hardness of the grains in the strongest orientation, H_{\min} is the average hardness of the grains in the weakest orientation and H_{all} is the average hardness computed for all indents at a given temperature. H_{\max} is always the average hardness of the grains indented parallel or subparallel to the c -axis ($[0001]$ or $\langle 22\bar{4}3 \rangle$). H_{\min} is always the average hardness of the grains indented in one of the two orientations normal to the c -axis ($\langle 11\bar{2}0 \rangle$ or $\langle 10\bar{1}0 \rangle$). At room temperature, the anisotropy of hardness is 10.0%.

Indentation hardness of calcite is also temperature dependent (Table 1 and Fig. 3). For orientations $[0001]$ and $\langle 22\bar{4}3 \rangle$ the hardness

decreases to 2.16 ± 0.08 and 2.17 ± 0.05 GPa, respectively, at 175 °C. Similarly, the hardness in the softer orientations, $\langle 11\bar{2}0 \rangle$ and $\langle 10\bar{1}0 \rangle$, decreases to 1.98 ± 0.11 and 1.98 ± 0.08 GPa, respectively, at 175 °C. The anisotropy of hardness at 175 °C is similar to that at room temperature, with a value of 9.2%.

Fig. 4 shows representative secondary electron images of the triangular indents produced by the three-sided pyramidal Berkovich probe. Indent size and depth both increase with temperature. The apothem and depth of room temperature indents are approximately 500 nm and 240–280 nm, respectively. The indents increase in size to an apothem of 750 nm and depths of 280–330 nm at 175 °C. At lower temperatures, the sides of indents performed in grains oriented with the indentation axis parallel or subparallel to the c -axis are rough and cracks are present. The most extreme cracking appears in grains indented parallel to the c -axis at room temperature (Fig. 4). As temperature increases, the number and density of cracks decreases and the sides of the indents become smoother. There are only a few cracks in indents performed at 125 °C and no cracks observed in indents performed at 175 °C. There is positive relief, referred to as ‘pile-up’, around the sides of the indents, formed by material that is displaced during indentation. SPM images in Fig. 5 show additional examples of this feature.

3.2 Micropillar compression

Fourteen micropillar compression experiments performed on pillars with a nominal diameter of 1 μm and oriented unfavorably for twinning (compression parallel to $\langle 22\bar{4}3 \rangle$) exhibit yield stresses varying from 0.82 to 1.15 GPa at 23 °C and 0.55–0.77 GPa at 175 °C. Pillars were examined before and after experiments to identify the mode of failure (Table 2). All pillars were characterized as having failed by brittle fracture, diffuse ductile deformation, or via deformation along shear bands. Brittle fracture was identified by the presence of open cracks. Diffuse ductile deformation was identified by a change in the shape of the pillar without any associated cracking or deformation along shear bands. Shear bands were identified in secondary electron images as narrow bands of high contrast.

Twelve 1 μm diameter pillars tested in grains oriented favorably for twinning (compression parallel to $\langle 10\bar{1}0 \rangle$) were more variable, with yield stresses ranging from 0.56 to 1.03 GPa at 23 °C and 0.27–0.72 GPa at 175 °C. All of the 1 μm pillars show either fracture or diffuse ductile deformation, without any noticeable shear bands (Table 2).

Additional micropillar compression experiments were conducted on 12 pillars with a diameter of 3 μm in both unfavorable (compression parallel to $\langle 22\bar{4}3 \rangle$) and favourable (compression parallel to $\langle 10\bar{1}0 \rangle$ and $\langle 11\bar{2}0 \rangle$) orientations for twinning. The yield stresses of the 6 pillars in the unfavorable orientation are comparable to those of the 1 μm pillars in the same orientation, ranging from 0.73 to 1.15 GPa. However, the 6 pillars tested in favourable orientations for twinning are markedly weaker than the 1 μm pillars tested under similar conditions, with yield stresses ranging from 0.10 to 0.36 GPa. The 3 μm pillars exhibit notably different deformation features from the 1 μm diameter pillars. While brittle and diffuse plastic deformation are observed in the 3 μm pillars, the larger samples also exhibit shear bands in the pillars favorably oriented for twinning that are not apparent in pillars unfavorably oriented for twinning (Fig. 6). STEM observation of these shear bands indicates that they are deformation twins on $e\{1018\}$. Fig. 7(a)

Table 1. Indentation hardness as a function of orientation and temperature.

| Temperature (°C) | Hardness (GPa) | | | | | | Anisotropy (%) |
|------------------|----------------|-------------|------------------------------|------------------------------|------------------------------|------------------------------|----------------|
| | All | [0001] | $\langle 22\bar{4}3 \rangle$ | $\langle 40\bar{4}1 \rangle$ | $\langle 11\bar{2}0 \rangle$ | $\langle 10\bar{1}0 \rangle$ | |
| 23 | 2.71 ± 0.15 | 2.82 ± 0.13 | 2.86 ± 0.13 | 2.71 ± 0.07 | 2.59 ± 0.10 | 2.60 ± 0.09 | 10.0 |
| 75 | 2.44 ± 0.11 | 2.54 ± 0.07 | 2.53 ± 0.08 | 2.42 ± 0.06 | 2.35 ± 0.07 | 2.35 ± 0.08 | 7.8 |
| 125 | 2.21 ± 0.11 | 2.34 ± 0.07 | 2.30 ± 0.06 | 2.19 ± 0.05 | 2.14 ± 0.08 | 2.11 ± 0.06 | 10.4 |
| 175 | 2.07 ± 0.12 | 2.16 ± 0.08 | 2.17 ± 0.05 | 2.05 ± 0.10 | 1.98 ± 0.11 | 1.98 ± 0.08 | 9.2 |

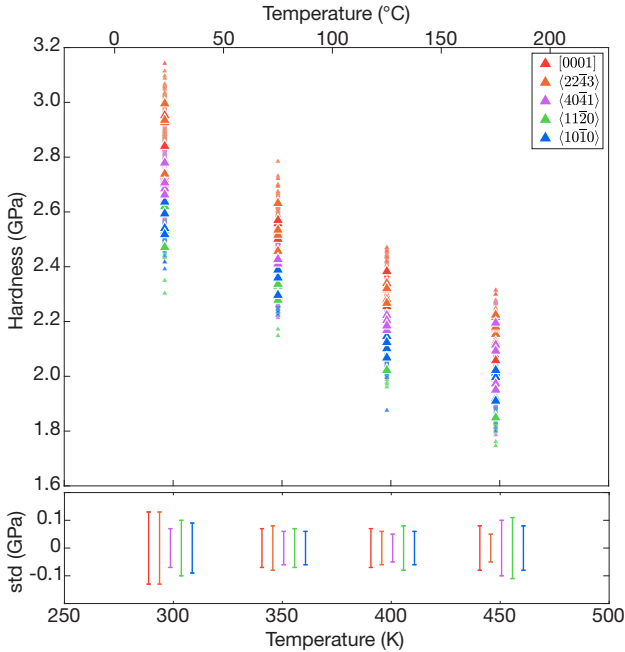


Figure 3. Indentation hardness plotted against temperature. Small triangles represent the individual indentations ($n = 2183$), and large triangles represent averages for 20–25 indentations performed in a single grain (colour corresponds to the orientation of the grain following the colour scheme in Fig. 1). Error bars in the bottom of the figure, which are offset for clarity, show \pm one standard deviation for each orientation.

shows a medium-angle annular dark field (MAADF) image of pillar 2086_P02, which is oriented nominally with the $m\{10\bar{1}0\}$ plane as its surface, with a shear band traversing across the pillar from top-left to bottom-right at an angle of $\sim 59^\circ$ from the horizontal. This angle is comparable to the known angle between m and e of $\sim 64^\circ$. Fig. 7(b) shows a high-angle annular dark field (HAADF) image of the pillar, with shear band highlighted as Region II, and either sides of the shear band highlighted as Regions I and III. Fig. 7(c) shows the fast Fourier transform (FFT) diffraction patterns of Regions I–III. We have used the crystal structure of calcite from Chessin *et al.* (1965) to index the FFT patterns. The FFT patterns confirm twinning during deformation, with an in-plane rotation of 43.78° for the shear band (Region II) with respect to the undeformed crystal on either side (Region I and II). This angle is close to the theoretical angle of 52.5° (Barber & Wenk 1979). The differences between the angles measured here and the theoretical angles are likely because the STEM foil was not cut perfectly orthogonal to the twin. The out of plane direction corresponds to $[\bar{2}201]$ orientation of calcite crystal structure (Chessin *et al.* 1965).

4 DISCUSSION

4.1 Yield stress from nanoindentation experiments

While indentation hardness measurements are precise and relatively straightforward to collect, there remains a significant challenge to scale these values to uniaxial properties used in traditional constitutive flow laws and models of deformation. To relate indentation hardness measurements to uniaxial mechanical properties, indentation hardness must be converted to yield stress, σ_y . This relationship is commonly expressed by a simple linear function, where hardness is proportional to yield stress via the constraint factor, C (eq. 8) (Tabor 1970).

$$H = C\sigma_y. \quad (8)$$

The constraint factor may vary from 1.1 to 3.0, where 1.1 represents the elastic limit, and 3.0 represents the plastic limit (Johnson 1970; Evans & Goetze 1979). Constraint factors are typically around 3 for materials with high E/σ_y ratios (> 133), such as metals, and can be as low as 1.5 for materials with low E/σ_y ratios, such as glasses and polymers (Swain & Hagan 1976; Fischer-Cripps 2011; Shaw & DeSalvo 2012). Calcite has a relatively low E/σ_y ratio, which means that the constraint factor is predicted to be in the range of $C = 1.5$ – 3.0 .

Multiple models have been used to estimate the constraint factor and yield stress. Here we present calculations for four such models: Johnson (1970), Evans & Goetze (1979), Mata *et al.* (2002), Mata & Alcalá (2003) and Ginder *et al.* (2018) (Table 3). As we have no independent constraint on the yield stress at these deformation conditions, we make no determination that one model is more valid than the others.

The first of these models, derived by Johnson (1970), compares indentation to an expanding cavity in an elastic–plastic solid. This method states that the ratio of indentation hardness to yield stress is determined by the geometry of the indenter and the elastic modulus of the material.

$$\frac{H}{\sigma_y} = \frac{2}{3} \left[1 + \ln \left(\frac{E \tan(\theta)}{\sigma_y} + 4(1 - 2\nu) \right) \right]. \quad (9)$$

Here, H is indentation hardness, σ_y is yield stress, E is Young’s modulus, ν is Poisson’s ratio and θ is the angle between the surface of a conical indenter and the indented surface. The value for θ can be adjusted to compensate for different indenter tip geometries by relating the volume of material displaced by differently shaped indenter probes (Fischer-Cripps 2011). We use eq. (9) to determine yield stress, though it can be simplified to eq. (10) if a Poisson’s ratio of 0.5 (i.e. an incompressible material) is assumed.

$$\frac{H}{\sigma_y} = \frac{2}{3} \left[1 + \ln \left(\frac{1}{3} \frac{E \tan(\theta)}{\sigma_y} \right) \right]. \quad (10)$$

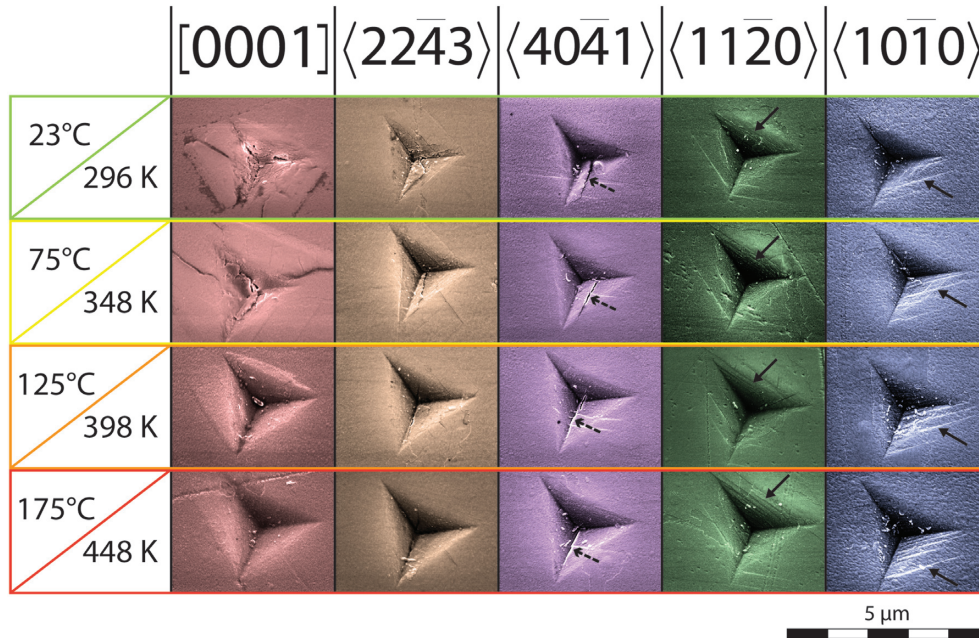


Figure 4. Array of representative secondary electron images of indentations at each temperature step (rows) and in each orientation (columns). Images are colored based on orientation following the colour scheme in Fig. 1. The size of the indentations increases with increasing temperature; apothems increase from 500 to 750 nm and depths increase from 240 to 330 nm from 23 to 175 °C. Linear cracks are present in each of the four images of indentations performed parallel to $\langle 40\bar{4}1 \rangle$ (marked by dashed arrows). All of these features appear in the same orientation, but do not appear to align with twin planes. The images of these indentations were taken after the sample was coated with iridium in preparation for micropillar fabrication, and these features are interpreted to be cracks or tears in the iridium coating caused by the SEM electron beam. There are bright linear features present in the lower, right-hand face of the indentations performed parallel to $\langle 10\bar{1}0 \rangle$, and dark linear features present in the upper face of the indentations performed parallel to $\langle 11\bar{2}0 \rangle$, though these are less prominent (marked by solid arrows). Due to the orientation of these grains and the fact that these features are not present in other grains, it is thought that these features are twin planes.

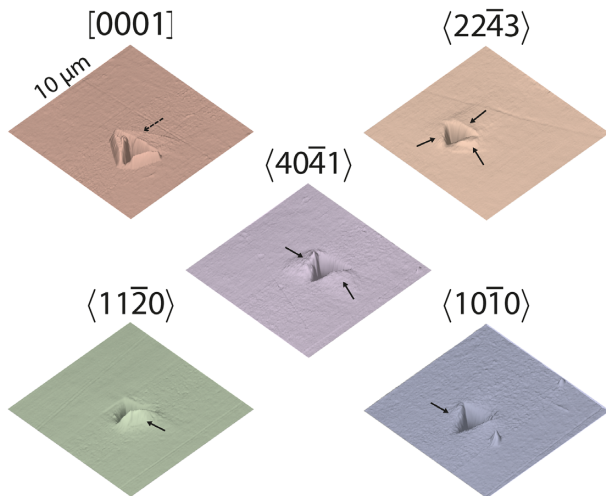


Figure 5. Scanning probe microscope (SPM) images of indentations made at room temperature in each orientation tested. Images are colored based on orientation following the colour scheme in Fig. 1. Pile up is observed in 4 of the 5 orientations (solid arrows) in varying amounts and on different sides of the indentation. This variation is due to the anisotropy of the calcite. Fractures are observed on the surface of the indentation parallel to $[0001]$ (dashed arrow).

Evans & Goetze (1979) determine an empirical model based on the expanding cavity model of Johnson (1970) using microindentation data in olivine. This model shows the same relationship between yield stress and indentation hardness as Johnson's model, though

with slightly different coefficients.

$$\frac{H}{\sigma_y} = 0.19 + 1.6 \log \left(\frac{E \tan(\theta)}{\sigma_y} \right). \quad (11)$$

Eq. (11) is used in combination with Tabor's eq. (8) to solve for yield stress and constraint factor simultaneously.

Mata *et al.* (2002) and Mata & Alcalá (2003) use finite element analysis to develop a new model for indentation in metals. Mata & Alcalá use Johnson's idea that the constraint factor is a function of the term, $\ln(E/\sigma_r)$, where σ_r is the reference stress at 10% strain. They then use finite element analysis to determine a polynomial function of $\ln(E/\sigma_r)$, which is used to solve for the reference stress.

$$\frac{H}{\sigma_r} = \sum_{i=0}^4 c_i \left[\ln \left(\frac{E}{\sigma_r} \right) \right]^i. \quad (12)$$

Here c_i are constants determined by the finite element analysis. This reference stress σ_r is comparable to the yield stresses determined by Johnson (1970), Evans & Goetze (1979), and Ginder *et al.* (2018). The reference stress is then used in conjunction with the curvature of the indentation load-displacement curve to determine a pile-up factor and work hardening exponent that are used to calculate yield stress. Due to these additional steps, the yield stress determined by Mata & Alcalá is approximately a factor of 4 lower than the reference stress. However, because the reference stress from Mata & Alcalá (2003) is defined the same way as the yield stresses from the other models, we use it in subsequent comparisons. This model was initially developed for materials with yield strengths between 50 and 1000 MPa and Young's moduli between 70 and 200 GPa. The results from our study show that yield stress for

Table 2. Micropillar compression results.

| Favorable for Twinning | | | | | | | | | |
|--------------------------|------------------------------------|----------------------------|--------------------------|------------------------------------|----------------------|--------|------------|---------|----------|
| Experiment Number | Compression Direction | Diameter (μm) | Height (μm) | Temperature ($^{\circ}\text{C}$) | Yield Strength (MPa) | | Yield Type | | |
| | | | | | First Test | Retest | Bands | Diffuse | Fracture |
| 1020_P01 ^a | $\langle 10\bar{1}0 \rangle$ | 1.3 | 2.2 | 23 | 0.466 | 0.661 | | | |
| 1020_P02 | $\langle 10\bar{1}0 \rangle$ | 1.3 | 2.1 | 23 | 0.78 | | | | |
| 1020_P05 | $\langle 10\bar{1}0 \rangle$ | 1.3 | 2.1 | 23 | 0.63 | | | | |
| 1020_P00 | $\langle 10\bar{1}0 \rangle$ | 1.4 | 2.1 | 23 | 1.04 | | | | |
| 1020_P06 | $\langle 10\bar{1}0 \rangle$ | 1.4 | 2.0 | 23 | 0.60 | | | | |
| 1020_P03 | $\langle 10\bar{1}0 \rangle$ | 1.4 | 2.1 | 23 | 0.32 | | | | |
| 1020_P04 ^a | $\langle 10\bar{1}0 \rangle$ | 1.4 | 2.0 | 23 | 0.88 | 0.56 | | | |
| 2086_P00 | $\langle 10\bar{1}0 \rangle$ | 2.6 | 7.0 | 23 | 0.16 | | | | |
| 2086_P01 | $\langle 10\bar{1}0 \rangle$ | 2.6 | 6.2 | 23 | 0.36 | | | | |
| 1018_P00 | $\langle 11\bar{2}0 \rangle$ | 3.0 | 6.7 | 23 | 0.16 | | | | |
| 1018_P01 | $\langle 11\bar{2}0 \rangle$ | 3.0 | 5.3 | 23 | 0.23 | | | | |
| 1018_P02 | $\langle 11\bar{2}0 \rangle$ | 3.0 | 6.3 | 23 | 0.10 | | | | |
| 1020_P10 ^a | $\langle 10\bar{1}0 \rangle$ | 1.3 | 2.0 | 175 | 0.35 | 0.57 | | | |
| 1020_P09 | $\langle 10\bar{1}0 \rangle$ | 1.3 | 2.1 | 175 | 0.51 | | | | |
| 1020_P08 | $\langle 10\bar{1}0 \rangle$ | 1.3 | 2.1 | 175 | 0.27 | | | | |
| 1020_P11 | $\langle 10\bar{1}0 \rangle$ | 1.3 | 2.1 | 175 | 0.72 | | | | |
| 1020_P07 ^b | $\langle 10\bar{1}0 \rangle$ | 1.4 | 2.1 | 175 | | 0.49 | | | |
| 2086_P02 | $\langle 10\bar{1}0 \rangle$ | 3.1 | 6.4 | 175 | 0.16 | | | | |
| Unfavorable for Twinning | | | | | | | | | |
| Experiment Number | Compression Direction | Diameter (μm) | Height (μm) | Temperature ($^{\circ}\text{C}$) | Yield Strength (MPa) | | Yield Type | | |
| | | | | | First Test | Retest | Bands | Diffuse | Fracture |
| 1005_P05 ^a | $\langle 2\bar{2}\bar{4}3 \rangle$ | 1.3 | 2.2 | 23 | 0.94 | 0.66 | | | |
| 1005_P08 | $\langle 2\bar{2}\bar{4}3 \rangle$ | 1.3 | 2.1 | 23 | 1.10 | | | | |
| 1005_P00 | $\langle 2\bar{2}\bar{4}3 \rangle$ | 1.3 | 2.1 | 23 | 0.93 | | | | |
| 1005_P01 | $\langle 2\bar{2}\bar{4}3 \rangle$ | 1.3 | 2.2 | 23 | 1.01 | | | | |
| 1005_P02 ^a | $\langle 2\bar{2}\bar{4}3 \rangle$ | 1.3 | 2.2 | 23 | 0.82 | N/A | | | |
| 1005_P03 | $\langle 2\bar{2}\bar{4}3 \rangle$ | 1.3 | 2.3 | 23 | 0.96 | | | | |
| 1005_P13 ^c | $\langle 2\bar{2}\bar{4}3 \rangle$ | 1.4 | 2.6 | 23 | | | | | |
| 1005_P04 ^a | $\langle 2\bar{2}\bar{4}3 \rangle$ | 1.4 | 2.0 | 23 | 0.88 | 0.77 | | | |
| 1008_P02 | $\langle 2\bar{2}\bar{4}3 \rangle$ | 2.9 | 5.6 | 23 | | | | | |
| 1008_P01 | $\langle 2\bar{2}\bar{4}3 \rangle$ | 3.0 | 6.2 | 23 | | | | | |
| 1008_P03 | $\langle 2\bar{2}\bar{4}3 \rangle$ | 3.0 | 6.4 | 23 | 0.73 | | | | |
| 1008_P04 | $\langle 2\bar{2}\bar{4}3 \rangle$ | 3.0 | 6.1 | 23 | 1.15 | | | | |
| 1008_P00 | $\langle 2\bar{2}\bar{4}3 \rangle$ | 3.0 | 6.2 | 23 | 1.05 | | | | |
| 1005_P12 ^a | $\langle 2\bar{2}\bar{4}3 \rangle$ | 1.4 | 2.2 | 23/175 ^d | 0.86 | 0.72 | | | |
| 1005_P06 | $\langle 2\bar{2}\bar{4}3 \rangle$ | 1.3 | 2.2 | 175 | N/A | | | | |
| 1005_P11 | $\langle 2\bar{2}\bar{4}3 \rangle$ | 1.3 | 2.0 | 175 | 0.76 | | | | |
| 1005_P10 ^b | $\langle 2\bar{2}\bar{4}3 \rangle$ | 1.3 | 2.0 | 175 | N/A | 0.77 | | | |
| 1005_P07 ^b | $\langle 2\bar{2}\bar{4}3 \rangle$ | 1.4 | 2.0 | 175 | N/A | 0.68 | | | |
| 1005_P09 ^b | $\langle 2\bar{2}\bar{4}3 \rangle$ | 1.4 | 2.2 | 175 | N/A | 0.55 | | | |
| 1008_P05 | $\langle 2\bar{2}\bar{4}3 \rangle$ | 3.1 | 6.7 | 175 | 1.11 | | | | |

^a A potential yield was observed and the initial test was stopped, however, after imaging the pillar, little to no deformation occurred.
^b Initial testing was stopped early due to a high instrument drift rate.
^c Pillar 1005_P13 was tested at a constant load of 1000 μN for 4 hours.
^d The initial test on pillar 1005_P12 was conducted at 23 $^{\circ}\text{C}$ and the second test was conducted at 175 $^{\circ}\text{C}$

calcite, as defined in Mata & Alcalá (2003) (~250 Mpa), is within the validated range, and that the Young’s modulus (50–65 GPa, depending on temperature and orientation) is just below the validated range.

Finally, Ginder *et al.* (2018) developed a model similar to that of Johnson (1970) but for a power-law creeping solid as opposed to an elastic–plastic solid. This method uses Johnson’s analysis of the dependence of indentation hardness on yield stress and Young’s

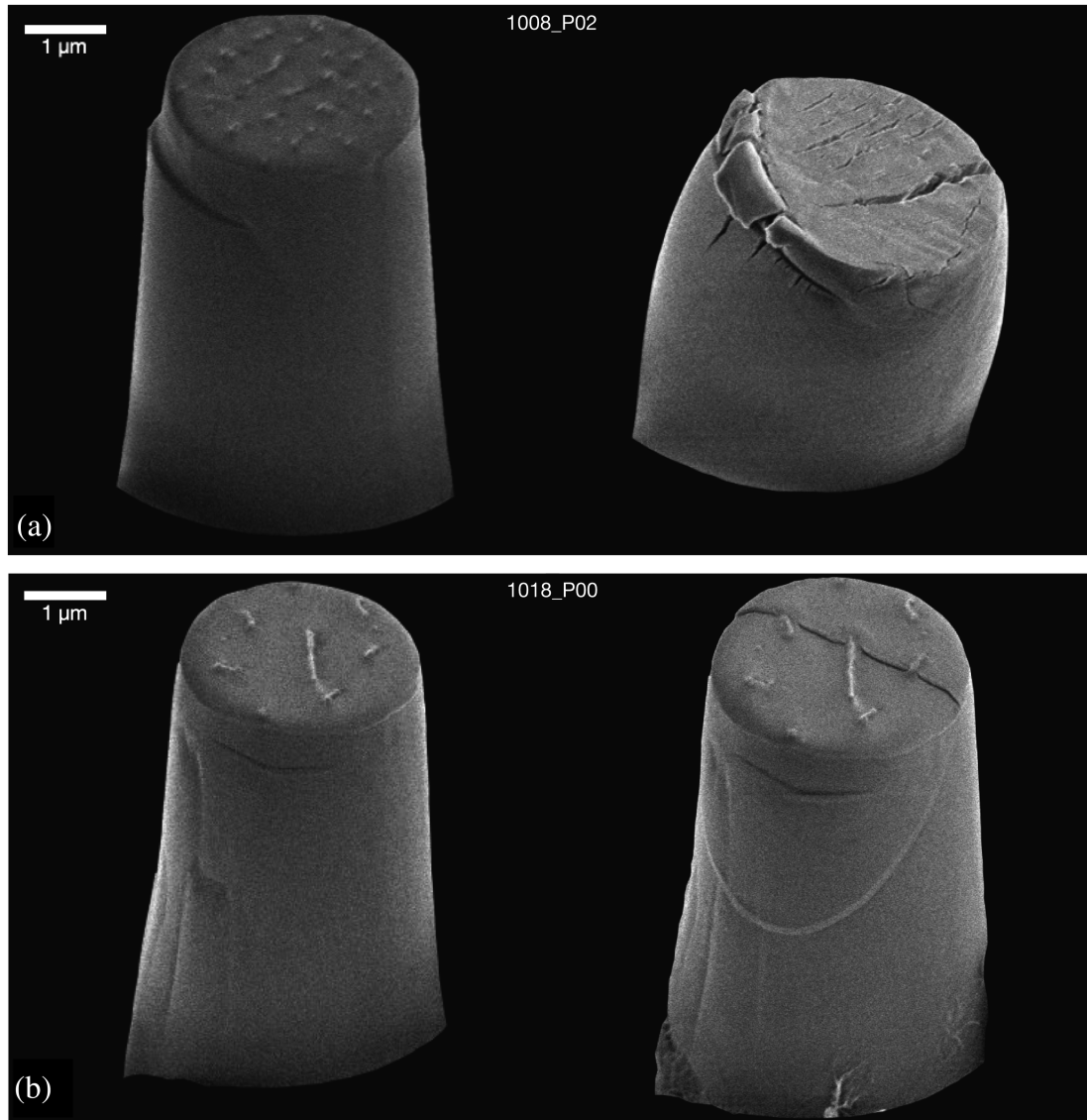


Figure 6. 3 μm diameter micropillars before (left-hand side) and after (right-hand side) a compression test. (a) A pillar oriented unfavorably for twinning (experiment 1008_PO2). The image taken after deformation shows that the pillar changed shape uniformly, exhibiting mainly diffuse ductile deformation with some minor fractures forming near the top of the pillar. (b) A pillar oriented favorably for twinning (experiment 1018_PO0). There is a shear band shown in bright relief at approximately a 45° angle to the axis of the pillar that appears after testing.

modulus during the indentation of an elastic–plastic solid (Johnson 1970) and simplifies the finite element model developed by Bower that takes a similar approach (Bower *et al.* 1993). Like Bower’s model, Ginder’s method correlates two power-law relationships: one for uniaxial compression, $\dot{\epsilon} = \alpha \sigma_y^n$, and one for indentation, $\dot{\epsilon}_i = \beta H^n$, where $\dot{\epsilon}$ is uniaxial strain rate, σ_y is yield stress, $\dot{\epsilon}_i$ is the indentation strain rate, H is the indentation hardness and n is the stress exponent. α and β are terms related to creep and indentation creep, respectively, and take an Arrhenius form. These expressions are related to one another by $\alpha = \beta F^n$, where F is the reduced contact pressure and a function of the stress exponent, n , derived from Johnson’s interpretation of the cavity expansion problem (Johnson 1970; Ginder *et al.* 2018). An explicit assumption in the Ginder model is that the rheology of the tested material is best modelled as a power law and is suitable for stress exponents less than ~ 7 . However, it is previously observed that the stress exponent of calcite is likely greater than 9 and may be as great as

70, even in experiments at high temperature (De Bresser & Spiers 1997). Higher stress exponents in the Ginder model results in lower calculated yield stresses. As such, we use a stress exponent of 7 in our calculation, which represents a conservative upper bound on the yield stress determined using the Ginder model.

4.2 Yield stress from micropillar compression

The 3 μm diameter pillars show a greater variation in yield stress with crystal orientation than the 1 μm diameter pillars. The yield stresses for the 1 μm pillars are distributed widely over the total range of yield stresses, while the 3 μm pillars show a distinct contrast between the pillars oriented favorably for twinning and those oriented unfavorably for twinning (Table 2). The differences are interpreted to be a consequence of the size of the micropillars; the 3 μm pillars are approximately 30 times larger in volume than the 1 μm pillars. Smaller pillars appear to suppress the formation of

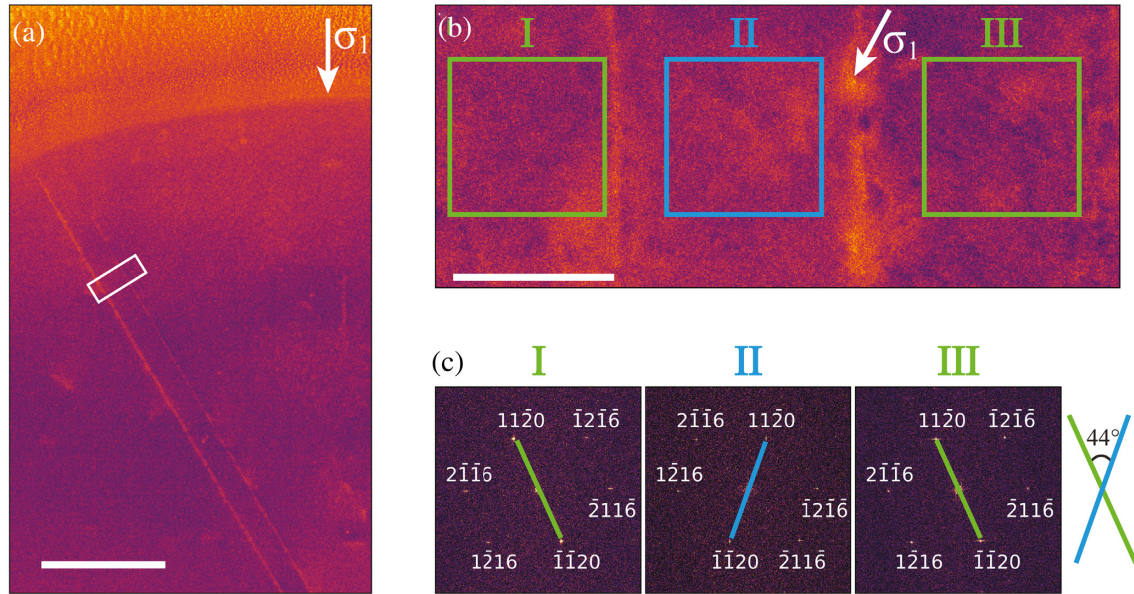


Figure 7. (a) A medium-angle annular dark field (MAADF) image of pillar 2086_P02 with a shear band traversing the pillar from the top left to bottom centre. The white box shows the area shown in (b). (b) A high-angle annular dark field (HAADF) image of the pillar rotated by 30°. Scale bars in A and B correspond to 300 and 30 nm, respectively Regions I and III are the undeformed regions of the material and region II is the twin. (c) Fast-Fourier transform patterns of Regions I, II and III, as highlighted in B. This shows an in-plane rotation of 44° between the twin, red, and the host, green. This angle differs from the theoretical angle of rotation because the sample was not perfectly orthogonal to the twin plane.

Table 3. Yield stress as a function of orientation and temperature of the four models used.

| Temperature (°C) | Yield Stress (GPa) (Johnson, 1970) | | | | | | Anisotropy (%) |
|------------------|------------------------------------|-------------|------------------------------|------------------------------|------------------------------|------------------------------|----------------|
| | All | [0001] | $\langle 22\bar{4}3 \rangle$ | $\langle 40\bar{4}1 \rangle$ | $\langle 11\bar{2}0 \rangle$ | $\langle 10\bar{1}0 \rangle$ | |
| 23 | 1.88 ± 0.19 | 1.99 ± 0.19 | 1.97 ± 0.11 | 1.83 ± 0.11 | 1.81 ± 0.17 | 1.84 ± 0.24 | 9.6 |
| 75 | 1.62 ± 0.15 | 1.73 ± 0.15 | 1.66 ± 0.10 | 1.55 ± 0.08 | 1.58 ± 0.18 | 1.60 ± 0.18 | 11.1 |
| 125 | 1.46 ± 0.16 | 1.60 ± 0.16 | 1.46 ± 0.09 | 1.39 ± 0.10 | 1.42 ± 0.15 | 1.43 ± 0.20 | 14.4 |
| 175 | 1.32 ± 0.13 | 1.43 ± 0.13 | 1.32 ± 0.08 | 1.28 ± 0.08 | 1.27 ± 0.10 | 1.32 ± 0.17 | 12.1 |

| Temperature (°C) | Yield Stress (GPa) (Evans & Goetze 1979) | | | | | | Anisotropy (%) |
|------------------|--|-------------|------------------------------|------------------------------|------------------------------|------------------------------|----------------|
| | All | [0001] | $\langle 22\bar{4}3 \rangle$ | $\langle 40\bar{4}1 \rangle$ | $\langle 11\bar{2}0 \rangle$ | $\langle 10\bar{1}0 \rangle$ | |
| 23 | 1.23 ± 0.10 | 1.30 ± 0.10 | 1.29 ± 0.06 | 1.21 ± 0.05 | 1.18 ± 0.09 | 1.20 ± 0.11 | 9.8 |
| 75 | 1.08 ± 0.08 | 1.14 ± 0.07 | 1.11 ± 0.05 | 1.04 ± 0.04 | 1.05 ± 0.09 | 1.06 ± 0.09 | 9.3 |
| 125 | 0.97 ± 0.08 | 1.05 ± 0.08 | 0.98 ± 0.04 | 0.94 ± 0.05 | 0.94 ± 0.07 | 0.94 ± 0.08 | 11.3 |
| 175 | 0.89 ± 0.06 | 0.95 ± 0.06 | 0.90 ± 0.04 | 0.87 ± 0.05 | 0.85 ± 0.05 | 0.88 ± 0.07 | 11.2 |

| Temperature (°C) | Yield Stress (GPa) (Mata & Alcala 2003) | | | | | | Anisotropy (%) |
|------------------|---|-------------|------------------------------|------------------------------|------------------------------|------------------------------|----------------|
| | All | [0001] | $\langle 22\bar{4}3 \rangle$ | $\langle 40\bar{4}1 \rangle$ | $\langle 11\bar{2}0 \rangle$ | $\langle 10\bar{1}0 \rangle$ | |
| 23 | 1.08 ± 0.06 | 1.12 ± 0.06 | 1.13 ± 0.05 | 1.07 ± 0.03 | 1.03 ± 0.04 | 1.04 ± 0.05 | 9.3 |
| 75 | 0.96 ± 0.04 | 1.01 ± 0.03 | 1.00 ± 0.03 | 0.95 ± 0.03 | 0.93 ± 0.04 | 0.93 ± 0.04 | 8.3 |
| 125 | 0.87 ± 0.04 | 0.93 ± 0.03 | 0.90 ± 0.03 | 0.86 ± 0.02 | 0.84 ± 0.03 | 0.84 ± 0.03 | 10.3 |
| 175 | 0.81 ± 0.05 | 0.85 ± 0.03 | 0.85 ± 0.03 | 0.80 ± 0.04 | 0.78 ± 0.04 | 0.78 ± 0.03 | 8.6 |

| Temperature (°C) | Yield Stress (GPa) (Ginder <i>et al.</i> 2018) | | | | | | Anisotropy (%) |
|------------------|--|-------------|------------------------------|------------------------------|------------------------------|------------------------------|----------------|
| | All | [0001] | $\langle 22\bar{4}3 \rangle$ | $\langle 40\bar{4}1 \rangle$ | $\langle 11\bar{2}0 \rangle$ | $\langle 10\bar{1}0 \rangle$ | |
| 23 | 0.83 ± 0.05 | 0.86 ± 0.04 | 0.87 ± 0.04 | 0.83 ± 0.02 | 0.79 ± 0.03 | 0.79 ± 0.03 | 9.6 |
| 75 | 0.74 ± 0.03 | 0.78 ± 0.02 | 0.77 ± 0.02 | 0.74 ± 0.02 | 0.72 ± 0.02 | 0.72 ± 0.02 | 8.1 |
| 125 | 0.68 ± 0.03 | 0.71 ± 0.02 | 0.70 ± 0.02 | 0.67 ± 0.02 | 0.65 ± 0.02 | 0.64 ± 0.02 | 10.3 |
| 175 | 0.63 ± 0.04 | 0.66 ± 0.02 | 0.66 ± 0.01 | 0.63 ± 0.03 | 0.60 ± 0.03 | 0.49 ± 0.02 | 27.0 |

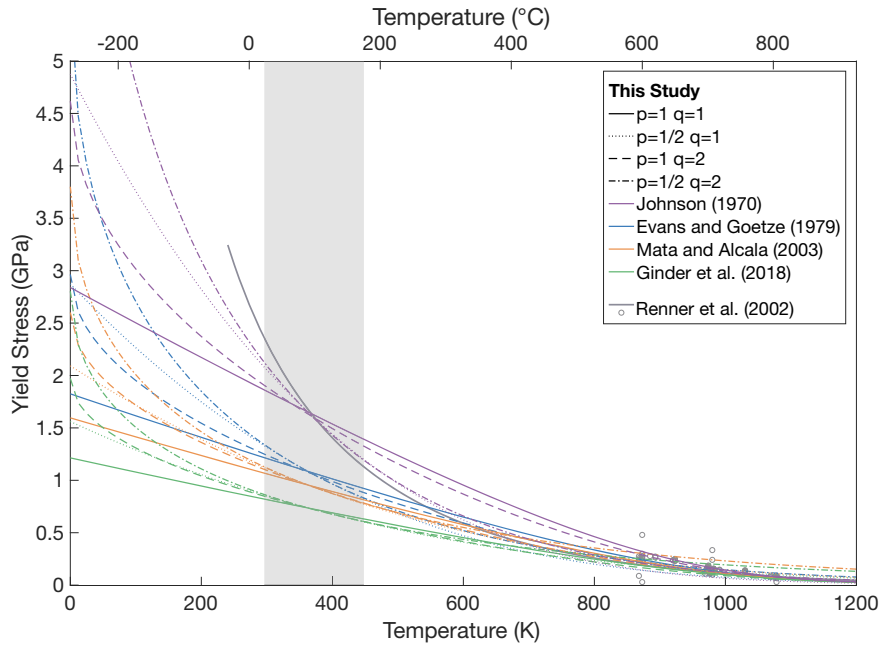


Figure 8. Several combinations of p and q were chosen for fitting eq. (13) for each of the four models described above. Resulting flow laws are shown as colored lines and fitting parameters are provided in Table 4. The shaded region shows the temperature range of our experiments. The flow laws from our study are in good agreement with higher temperature results from Renner *et al.* (2002), shown in grey circles.

twins and shear bands and are inferred to exhibit more stochastic behavior, resulting in a wider range of yield stresses (Table 2). Similar stochastic behavior has been observed in metallic glasses (Bharathula *et al.* 2010). The variation in yield stresses of the 1 μm pillars could also be due to differences in defect density from pillar to pillar, or a preexisting twin in the micropillar. The 3 μm pillars may have a more representative defect density making their behavior more predictable. The difference in yield stresses between favorably and unfavorably oriented 3 μm pillars is interpreted to be due to the ease of deformation twinning in the favorably oriented pillars. Other slip systems, namely $r\{10\bar{1}4\}\langle\bar{2}201\rangle$ and $f\{\bar{1}012\}\langle\bar{2}201\rangle$, require higher stresses to activate than the twin system (De Bresser & Spiers 1997). The yield stresses in pillars oriented favorably for twinning are on average $\sim 50\%$ lower than the yield stresses calculated from indentation in grains of similar orientations, while the pillars oriented unfavorably for twinning show similar, though still slightly lower, yield stresses to their indentation counterparts. This is likely caused by the geometry of the sample and the number of active slip systems required for plastic deformation. It is assumed that secondary slip systems are activated during indentation experiments, which are needed to accommodate the spherical pattern of deformation. In contrast, a micropillar may require only one slip system (Evans & Goetze 1979). Hence, we conclude that the yield stresses determined for the twinned micropillars represent a lower limit on the rheology of calcite and are in general agreement with the data obtained from nanoindentation experiments.

4.3 Low-temperature flow laws

We fit our indentation data to a flow law for plasticity limited by lattice resistance [from eq. 2.12 from Frost & Ashby (1982)]:

$$\dot{\epsilon} = A\sigma_y^2 \exp\left\{-\frac{H^*}{RT}\left[1 - \left(\frac{\sigma_y}{\sigma_p}\right)^p\right]^q\right\}, \quad (13)$$

where $\dot{\epsilon}$ is strain rate, A is a pre-exponential factor, H^* is the activation enthalpy, R is the gas constant, T is temperature, σ_y is yield stress, σ_p is athermal Peierls stress and p and q are dimensionless quantities that depend on the energy barriers to dislocation motion with values $0 < p \leq 1$ and $1 \leq q \leq 2$ (Kocks *et al.* 1975). Calculated yield stresses and strain rates for several predefined values for p and q are used to fit the athermal Peierls stress, σ_p , and A , to eq. (13) (Table 2 and Fig. 8). A value of activation enthalpy, H^* , of 200 kJ mol^{-1} has been determined in a previous study and is used to fit the data here (Renner *et al.* 2002). Values for A of $6.4 \times 10^5 - 2.0 \times 10^{10} \text{ GPa}^{-2}\text{s}^{-1}$ and σ_p of 1.2–9.9 GPa were calculated using MATLAB's Curve Fitting Tool.

4.4 Size effect

Additional indentation experiments were conducted over a range of maximum loads of 0.1–25 mN in five individual grains to investigate the effect of contact radius on indentation hardness. The maximum loads correspond to contact radii ranging from 0.2 to 1.8 μm . These tests show a weak dependence of indentation hardness on contact area of the form $H \propto a_c^m$, with $m = -0.05$ (Fig. 9). a_c is the contact radius defined by: $a_c = h_c \tan(\theta)$ where h_c is the contact depth of a given indent and θ is the effective cone angle of a Berkovich tip (Fischer-Cripps 2011). The majority of the curvature observed in this study occurs at very small contact radii and indentation hardness remains fairly constant for contact radii $\geq \sim 1 \mu\text{m}$. While the effect of indentation size on hardness is minor, additional tests at higher loads or with larger indenter tips are necessary to fully understand the indentation size effect in calcite.

Given that the maximum load for all indents in this study was set to a constant value of 5 mN, the size effect does not affect the results of our study. For a given maximum load, differences in contact radius reflect differences in indentation hardness and by extension yield stress.

Table 4. Flow law parameters.

| | $p = 1, q = 1$ | $p = 1/2, q = 1$ | $p = 1, q = 2$ | $p = 1/2, q = 2$ |
|--|---|---|---|---|
| Johnson (1970) | | | | |
| A (Gpa ⁻² s ⁻¹) | $2.00 \times 10^{10} \begin{smallmatrix} 3.50 \times 10^{10} \\ 5.00 \times 10^9 \end{smallmatrix}$ | $2.00 \times 10^{10} \begin{smallmatrix} 3.87 \times 10^{10} \\ 1.35 \times 10^9 \end{smallmatrix}$ | $2.00 \times 10^{10} \begin{smallmatrix} 3.80 \times 10^{10} \\ 2.03 \times 10^9 \end{smallmatrix}$ | $8.13 \times 10^8 \begin{smallmatrix} 1.75 \times 10^9 \\ 1.20 \times 10^8 \end{smallmatrix}$ |
| σ_p (GPa) | $2.84 \begin{smallmatrix} 2.90 \\ 1.86 \end{smallmatrix}$ | $4.88 \begin{smallmatrix} 5.12 \\ 4.63 \end{smallmatrix}$ | $4.62 \begin{smallmatrix} 4.76 \\ 4.47 \end{smallmatrix}$ | $10.73 \begin{smallmatrix} 11.54 \\ 9.91 \end{smallmatrix}$ |
| Evans & Goetze (1979) | | | | |
| A (Gpa ⁻² s ⁻¹) | $2.00 \times 10^{10} \begin{smallmatrix} 3.35 \times 10^{10} \\ 6.53 \times 10^9 \end{smallmatrix}$ | $5.17 \times 10^9 \begin{smallmatrix} 9.39 \times 10^9 \\ 9.60 \times 10^8 \end{smallmatrix}$ | $2.00 \times 10^{10} \begin{smallmatrix} 3.63 \times 10^{10} \\ 3.74 \times 10^9 \end{smallmatrix}$ | $5.13 \times 10^7 \begin{smallmatrix} 9.88 \times 10^7 \\ 3.81 \times 10^6 \end{smallmatrix}$ |
| σ_p (GPa) | $1.82 \begin{smallmatrix} 1.86 \\ 1.79 \end{smallmatrix}$ | $2.04 \begin{smallmatrix} 2.07 \\ 2.01 \end{smallmatrix}$ | $2.99 \begin{smallmatrix} 3.05 \\ 2.88 \end{smallmatrix}$ | $5.64 \begin{smallmatrix} 5.97 \\ 3.31 \end{smallmatrix}$ |
| Mata & Alcalá (2003) | | | | |
| A (Gpa ⁻² s ⁻¹) | $2.00 \times 10^{10} \begin{smallmatrix} 3.13 \times 10^{10} \\ 8.74 \times 10^9 \end{smallmatrix}$ | $1.16 \times 10^8 \begin{smallmatrix} 1.85 \times 10^8 \\ 4.67 \times 10^7 \end{smallmatrix}$ | $2.00 \times 10^{10} \begin{smallmatrix} 3.47 \times 10^{10} \\ 5.29 \times 10^9 \end{smallmatrix}$ | $7.94 \times 10^5 \begin{smallmatrix} 1.32 \times 10^6 \\ 2.67 \times 10^5 \end{smallmatrix}$ |
| σ_p (GPa) | $1.60 \begin{smallmatrix} 1.62 \\ 1.57 \end{smallmatrix}$ | $2.09 \begin{smallmatrix} 2.15 \\ 2.03 \end{smallmatrix}$ | $2.60 \begin{smallmatrix} 2.67 \\ 2.54 \end{smallmatrix}$ | $3.80 \begin{smallmatrix} 3.96 \\ 3.64 \end{smallmatrix}$ |
| Ginder <i>et al.</i> (2018) | | | | |
| A (Gpa ⁻² s ⁻¹) | $2.00 \times 10^{10} \begin{smallmatrix} 3.09 \times 10^{10} \\ 9.07 \times 10^9 \end{smallmatrix}$ | $9.33 \times 10^7 \begin{smallmatrix} 1.47 \times 10^8 \\ 3.99 \times 10^7 \end{smallmatrix}$ | $2.00 \times 10^{10} \begin{smallmatrix} 3.46 \times 10^{10} \\ 5.44 \times 10^9 \end{smallmatrix}$ | $6.38 \times 10^5 \begin{smallmatrix} 1.04 \times 10^6 \\ 2.33 \times 10^5 \end{smallmatrix}$ |
| σ_p (GPa) | $1.21 \begin{smallmatrix} 1.23 \\ 1.20 \end{smallmatrix}$ | $1.56 \begin{smallmatrix} 1.60 \\ 1.52 \end{smallmatrix}$ | $1.97 \begin{smallmatrix} 2.02 \\ 1.92 \end{smallmatrix}$ | $2.80 \begin{smallmatrix} 2.92 \\ 2.69 \end{smallmatrix}$ |

Values for the preexponential, A , and athermal Peierls stress, σ_p , are shown for each set of p and q . 95% confidence intervals are shown as super- and subscripts representing the positive and negative confidence intervals, respectively.

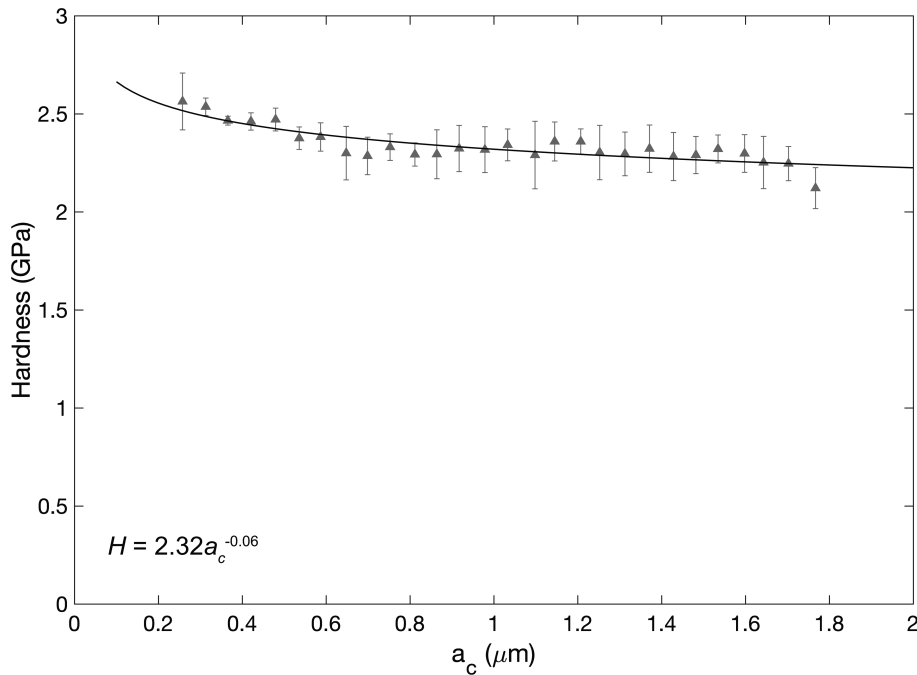


Figure 9. Indentation experiments done over a range of contact radii to look at the effect of indent size on indentation hardness. Indentation experiments were binned based on indentation contact depth into 20 nm bins, then converted to contact radius. The average (grey triangles) and standard deviation (error bars) for indentation hardness in each bin are shown. From this we see that the majority of the size effect appears at very low contact radii, but $a_c > \sim 0.8$ shows little variation. A power-law relationship is fit to the data (black line) and gives a relationship of $H = 2.32a_c^{-0.06}$.

4.5 Comparison to previous studies

At temperatures greater than ~ 800 °C, the four different models used to determine yield stress are in good agreement with one another (Fig. 8). Moreover, the yield stresses obtained through these calculations are broadly consistent with the results from triaxial deformation experiments by Renner & Evans (2002), when extrapolated to the temperature range and strain-rates used in that study. Renner's study was conducted using synthetic polycrystal calcite samples with grain sizes ranging from ~ 6 to > 65 μm , at strain rates of 5×10^{-7} – 3×10^{-3} s^{-1} and temperatures of 600–800 °C. Extrapolating Renner's results to the higher strain-rates of this study, the yield stresses range from ~ 250 MPa at 600 °C down to ~ 80 MPa at 800 °C (Fig. 8). The athermal Peierls stresses

calculated by Renner *et al.* (2002) (≈ 0.47 – 1.5 GPa depending on grain size) are lower than those determined in this study. The difference is likely due to the different temperature ranges in each study: much of the curvature of the flow law occurs at low temperatures ($T < \sim 500$ K), which makes it difficult to constrain the athermal Peierls stress using only data from experiments at $T > 800$. Furthermore, differences in the formulation of the low temperature plastic flow laws may explain some differences in the calculated flow law parameters. Renner *et al.* (2002) define their flow law as:

$$\dot{\epsilon} = A\sigma_y^2 \exp\left(\frac{\sigma_y}{\sigma_p} - \frac{Q}{RT}\right), \quad (14)$$

where Q is activation energy and σ_p includes a temperature dependent Peierls stress as well as a grain size dependent term (Renner &

Evans 2002; Renner *et al.* 2002). All other parameters are the same as in eq. (4.3). This formulation allows the yield stress to exceed the athermal Peierls stress given a finite strain rate at $T = 0$ K, whereas eq. (4.3) requires $\sigma_y = \sigma_p$ at $T = 0$ K. Although our flow laws agree with the results from Renner *et al.* (2002) at higher temperature ($T > 800$ K), it is also likely that different deformation mechanisms are active in the two studies, dislocation creep in the study by Renner *et al.* (2002) and low temperature plasticity in our study, and that direct comparison may not be appropriate.

The results from our study are less consistent with the results from studies by Turner *et al.* (1954) and De Bresser & Spiers (1997), who performed uniaxial and triaxial compression experiments on calcite single crystals. Turner *et al.* (1954) performed triaxial deformation experiments from 20 to 400 °C, confining pressure from 0.3 to 1.0 GPa, and strain rates of 2.5×10^{-5} s⁻¹ in single crystals of calcite oriented favorably and unfavorably for twinning. In the samples favorably oriented for twinning, the yield stresses (~15 MPa), once extrapolated to higher strain rates using the power-law expression $\dot{\epsilon} \propto \sigma^n$, where n ranges from 9.3 to 71.7 (De Bresser Spiers 1997), are still an order of magnitude lower than the yield stresses of the 3 μ m diameter micropillars favorably oriented for twinning (~150 MPa) and close to two orders of magnitude lower than the yield stresses calculated from indentation experiments (~1 GPa) at room temperature. The unfavorably oriented samples tested by Turner exhibit yield stresses of ~350 MPa at room temperature, which is about a factor of three smaller than the results from both the micropillar compression experiments and the indentation experiments (~1 GPa). The anisotropy observed in Turner *et al.*'s work is greater than the anisotropy observed in our nanoindentation experiments. We attribute this to the complex stress state during the indentation test, which requires multiple active slip systems to activate in order for deformation to occur. In contrast, a single slip, or twin system can accommodate the majority of the deformation in uniaxial and triaxial deformation experiments on single crystals.

De Bresser & Spiers (1997) conducted uniaxial compression experiments on calcite single crystals at temperatures ranging from 300 to 800 °C and strain rates of 3×10^{-4} – 3×10^{-8} s⁻¹. Yield stresses measured in their study are a factor of 5 less than the yield stresses determined in this study, even after correcting for the difference in strain rate using the same power-law relationship as above. The scale of the samples in the studies by Turner and De Bresser and Spiers—approximately 12 mm in diameter—may be one reason for the inconsistencies between the results from our study and theirs. Further investigation is needed to understand the role of sample size.

5 CONCLUSIONS

This study used methods from materials science, including nanoindentation and the first known application of micropillar compression testing in geologic materials, to constrain the rheology of calcite at low temperatures. The yield stress of calcite depends on both temperature and orientation; however, the temperature dependence is the dominant effect. The data collected in this study agree generally with the data and flow law from previous work (Renner *et al.* 2002). These data also provide flow laws that are more confidently extrapolated to low temperatures at which natural deformation has been observed. The athermal Peierls stress for calcite is determined by these flow laws to be 1.2–9.9 GPa depending on which model is used to convert indentation hardness to uniaxial yield stress, and which values of p and q are selected. The flow laws obtained here

can be used to constrain the rheology of calcite at temperatures from 23 to 175 °C, thus improving the interpretation of data from naturally deformed calcite rocks.

ACKNOWLEDGEMENTS

This work is funded by NSF EAR 1726165. Instrument support is provided by the Institute of Materials Science and Engineering at Washington University in St Louis. STEM sample preparation was conducted at the Center for Nanophase Materials Sciences at Oak Ridge National Laboratory (ORNL), which is a Department of Energy (DOE) Office of Science User Facility, through a user project (A.S.T. and R.M.). Microscopy work performed at ORNL was supported by the U.S. DOE, Office of Science, Basic Energy Sciences Materials Science and Engineering Division (BES-MSED). We would like to thank Andreas Kronenberg and two anonymous reviewers for their helpful and insightful comments.

REFERENCES

- Barber, D.J. & Wenk, H.R., 1979. Deformation twinning in calcite, dolomite, and other rhombohedral carbonates, *Phys. Chem. Miner.*, **5**, 141–165.
- Barnhoorn, A., Bystricky, M., Burlini, L. & Kunze, K., 2004. The role of recrystallisation on the deformation behaviour of calcite rocks: large strain torsion experiments on Carrara marble, *J. Struct. Geol.*, **26**, 885–903.
- Bharathula, A., Lee, S.W., Wright, W.J. & Flores, K.M., 2010. Compression testing of metallic glass at small length scales: effects on deformation mode and stability, *Acta Mater.*, **58**, 5789–5796.
- Bower, A.F., Fleck, N.A., Needleman, A. & Ogbonna, N., 1993. Indentation of a power law creeping solid, *R. Soc.*, **441 A**, 97–124.
- De Bresser, J.H.P., 1996. Steady state dislocation densities in experimentally deformed calcite materials: single crystal versus polycrystals, *J. geophys. Res.*, **101**, 22 189–22 201.
- De Bresser, J.H.P., Evans, B. & Renner, J., 2002. On estimating the strength of calcite rocks under natural conditions, *Geol. Soc. Lond., Spec. Publ.*, **200**, 309–329.
- De Bresser, J.H.P. & Spiers, C.J., 1990. High-temperature deformation of calcite single crystals by r+ and f+ slip, *Geol. Soc. Lond., Spec. Publ.*, **54**, 285–298.
- De Bresser, J.H.P. & Spiers, C.J., 1997. Strength characteristics of the r, f, and c slip systems in calcite, *Tectonophysics*, **272**, 1–23.
- De Bresser, J.H.P., Spiers, C.J., De Bresser, J.H.P. & Spiers, C.J., 1993. Slip systems in calcite single crystals deformed at 300–800 °C, *J. geophys. Res.*, **98**, 6397–6409.
- Burkhard, M., 2000. Calcite twins, their geometry, appearance and significance as stress-strain markers and indicators of tectonic regime: a review, *J. Struct. Geol.*, **15**, 351–368.
- Chessin, H., Hamilton, W.C. & Post, B., 1965. Position and thermal parameters of oxygen atoms in calcite, *Acta Crystallogr.*, **18**, 689–693.
- Evans, B. & Goetze, C., 1979. The temperature variation of hardness of olivine and its implication for polycrystalline yield stress, *J. geophys. Res.*, **84**, 5505.
- Ferrill, D.A., Morris, A.P., Evans, M.A., Burkhard, M., Groshong, R.H. & Onasch, C.M., 2004. Calcite twin morphology: a low-temperature deformation geothermometer, *J. Struct. Geol.*, **26**, 1521–1529.
- Fischer-Cripps, A.C., 2011. *Nanoindentation*, eds Winer, W.O. *et al.*, 3rd edn, Springer.
- Fredrich, J.T., Evans, B. & Wong, T.-F., 1989. Brittle to plastic transition in Carrara Marble, **94**, 4129–4145.
- Fredrich, J.T., Evans, B. & Wong, T.-F., 1990. Effect of grain size on brittle and semibrittle strength: implications for micromechanical modeling of failure in compression, *J. geophys. Res.*, **95**, 10 907–10 920.
- Frost, H.J. & Ashby, F., 1982. *Deformation-Mechanism Maps: The Plasticity and Creep of Metals and Ceramics*, Pergamon Press.
- Ginder, R.S., Nix, W.D. & Pharr, G.M., 2018. A simple model for indentation creep, *J. Mech. Phys. Solids*, **112**, 552–562, Elsevier Ltd.

- Goldsby, D.L., Rar, A., Pharr, G.M. & Tullis, T.E., 2004. Nanoindentation creep of quartz, with implications for rate- and state-variable friction laws relevant to earthquake mechanics, *J. Mater. Res.*, **19**, 357–365.
- Griggs, D.T., Turner, F.J. & Heard, H.C., 1960. Chapter 4: deformation of rocks at 500° to 800° C, *Geol. Soc. Am. Mem.*, **79**, 39–104.
- Hirth, G. & Kohlstedt, D.L., 2015. The stress dependence of olivine creep rate: Implications for extrapolation of lab data and interpretation of recrystallized grain size, *Earth planet. Sci. Lett.*, **418**, 20–26.
- Johnson, K.L., 1970. The correlation of indentation experiments, *J. Mech. Phys. Solids*, **18**, 115–126.
- Kearney, C., Zhao, Z., Bruet, B.J.F., Radovitzky, R., Boyce, M.C. & Ortiz, C., 2006. Nanoscale anisotropic plastic deformation in single crystal aragonite, *Phys. Rev. Lett.*, **255505**, 1–4.
- Kennedy, L.A. & White, J.C., 2001. Low-temperature recrystallization in calcite: mechanisms and consequences, *Geology*, **29**, 1027–1030.
- Kim, S., Ree, J., Han, R., Kim, N. & Jung, H., 2018. Tectonophysics Fabric transition with dislocation creep of a carbonate fault zone in the brittle regime, *Tectonophysics*, **723**, 107–116.
- Kocks, U.F., Argon, A.S. & Ashby, M.F., 1975, *Thermodynamics and Kinetics of Slip*, Pergamon Press.
- Korte-Kerzel, S., 2017. Microcompression of brittle and anisotropic crystals: recent advances and current challenges in studying plasticity in hard materials, *MRS Commun.*, **7**, 1–12.
- Korte, S. & Clegg, W.J., 2009. Micropillar compression of ceramics at elevated temperatures, *Scr. Mater.*, **60**, 807–810.
- Kranjc, K., Rouse, Z., Flores, K.M. & Skemer, P., 2016. Low-temperature plastic rheology of olivine determined by nanoindentation, *Geophys. Res. Lett.*, **42**, 176–184.
- Kumamoto, K.M. *et al.*, 2017. Size effects resolve discrepancies in 40 years of work on low-temperature plasticity in olivine, *Sci. Adv.*, **3**, 1–7.
- Liu, J., Walter, J.M. & Weber, K., 2002. Fluid-enhanced low-temperature plasticity of calcite marble: Microstructures and mechanisms, *Geology*, **787–790**.
- Mei, S., Suzuki, A.M., Kohlstedt, D.L., Dixon, N.A. & Durham, W.B., 2010. Experimental constraints on the strength of the lithospheric mantle, *J. geophys. Res.*, **115**, 1–9.
- Negrini, M., Smith, S.A.F., Scott, J.M., Tarling, M.S. & Irene, M., 2018. Microstructural and rheological evolution of calcite mylonites during shear zone thinning: constraints from the Mount Irene shear zone, Fiordland, New Zealand, *J. Struct. Geol.*, **106**, 86–102.
- Oliver, W.C. & Pharr, G.M., 1992. An improved technique for determining hardness and elastic modulus using load and displacement sensing indentation experiments, *J. Mater. Res.*, **7**, 1564–1583.
- Oliver, W.C. & Pharr, G.M., 2004. Measurement of hardness and elastic modulus by instrumented indentation: Advances in understanding and refinements to methodology, *J. Mater. Res.*, **19**, 3–20.
- Pieri, M., Burlini, L., Kunze, K., Stretton, I. & Olgaard, D.L., 2001. Rheological and microstructural evolution of Carrara marble with high shear strain: results from high temperature torsion experiments, *J. Struct. Geol.*, **23**, 1393–1413.
- Pieri, M., Kunze, K., Burlini, L., Stretton, I., Olgaard, D.L., Purg, J.-P. & Wenk, H.-R., 2001. Texture development of calcite by deformation and dynamic recrystallization at 1000 K during torsion experiments of marble to large strains, *Tectonophysics*, **330**, 119–140.
- Platt, J.P. & De Bresser, J.H.P., 2017. Stress dependence of microstructures in experimentally deformed calcite, *J. Struct. Geol.*, **105**, 80–87.
- Renner, J. & Evans, B., 2002. Do calcite rocks obey the power-law creep equation? *Geol. Soc. Lond., Spec. Publ.*, **200**, 293–307.
- Renner, J., Evans, B. & Siddiqi, G., 2002. Dislocation creep of calcite, *J. geophys. Res.*, **107**, ECV 6–1-ECV 6-16.
- Rowe, K.J. & Rutter, E.H., 1990. Palaeostress estimation using calcite twinning: experimental calibration and application to nature, *J. Struct. Geol.*, **12**, 1–17.
- Rutter, E.H., 1995. Experimental study of the influence of stress, temperature, and strain on the dynamic recrystallization of Carrara marble, *J. geophys. Res.*, **100**, 651–663.
- Rybacki, E., Janssen, C., Wirth, R., Chen, K., Wenk, H.R., Stromeyer, D. & Dresen, G., 2011. Low-temperature deformation in calcite veins of SAFOD core samples (San Andreas Fault. - Microstructural analysis and implications for fault rheology, *Tectonophysics*, **509**, 107–119.
- Schmid, S.M., Panozzot, R. & Bauer, S., 1987. Special Research Paper * Simple shear experiments on calcite rocks: rheology and microfabric, *J. Struct. Geol.*, **9**, 747–778.
- Schuster, R., Scha, E., Schell, N., Kunz, M. & Abart, R., 2017. Microstructure of calcite deformed by high-pressure torsion: an X-ray line profile study, *Tectonophysics*, **721**, 448–461.
- Shaw, M.C. & DeSalvo, G.J., 2012. The role of elasticity in hardness testing, *Metallogr. Microstruct. Anal.*, **1**, 310–317.
- Swain, M. V. & Hagan, J.T., 1976. Indentation plasticity and the ensuing fracture of glass, *J. Phys. D. Appl. Phys.*, **9**, 2201–2214.
- Tabor, D., 1970. The hardness of solids, *Rev. Phys. Technol.*, **1**, 145. Retrieved from <http://stacks.iop.org/0034-6683/1/i=3/a=101>
- Thom, C. & Goldsby, D., 2019. Nanoindentation studies of plasticity and dislocation creep in halite, *Geosciences*, **9**, 79.
- Turner, F.J., Griggs, D.T. & Heard, H., 1954. Experimental deformation of calcite crystals, *Bull. Geol. Soc. Am.*, **65**, 883–934.
- Uchic, M.D., Shade, P.A. & Dimiduk, D.M., 2009. Plasticity of micrometer-scale single crystals in compression, *Annu. Rev. Mater. Res.*, **39**, 361–386.
- VanLandingham, M.R., 2003. Review of instrumented indentation, *J. Res. Natl. Inst. Stand. Technol.*, **108**, 249.
- Verberne, B.A., De Bresser, J.H.P., Niemeijer, A.R., Spiers, C.J., Winter, D.A.M. & Plümpner, O., 2013. Nanocrystalline slip zones in calcite fault gouge show intense crystallographic preferred orientation: crystal plasticity at sub-seismic slip rates at 18–150° C, *Geology*, **41**(8), 863–866.
- Vernon, R.H., 1981. Optical microstructure of partly recrystallized calcite in some naturally deformed marbles, *Tecto*, **78**, 601–612.
- Wells, R.K., Newman, J. & Wojtal, S., 2014. Microstructures and rheology of a calcite-shale thrust fault, *J. Struct. Geol.*, **65**, 69–81.
- Xu, L. & Evans, B., 2010. Strain heterogeneity in deformed Carrara marble using a microscale strain mapping technique, *J. geophys. Res.*, **115**, B04202, doi:10.1029/2009JB006458.
- Mata, M., Anglada, M. & Alcalá, J., 2002. Contact deformation regimes around sharp indentations and the concept of the characteristic strain, *Journal of Materials Research*, **17**, 964–976.
- Mata, M. & Alcalá, J., 2003. Mechanical property evaluation through sharp indentations in elastoplastic and fully plastic contact regimes, *Journal of Materials Research*, **18**, 1705–1709.